Optical Materials 78 (2018) 325–334

Contents lists available at ScienceDirect

Optical Materials

journal homepage: www.elsevier.com/locate/optmat

Nanostructured zinc oxide photoelectrodes by green routes M-SILAR and electrodeposition for dye sensitized solar cell

M.A. Gaikwad [a], M.P. Suryawanshi [b], P.S. Maldar [a], T.D. Dongale [c], A.V. Moholkar [a, *]

[a] *Thin Film Nanomaterials Laboratory, Department of Physics, Shivaji University, Kolhapur 416-004, M. S., India*
[b] *Optoelectronics Convergence Research Center, Department of Materials Science and Engineering, Chonnam National University, 300, Yongbong-Dong, Buk-Gu, Gwangju 500-757, South Korea*
[c] *School of Nanoscience and Biotechnology, Shivaji University, Kolhapur 416-004, M. S., India*

ARTICLE INFO

Article history:
Received 11 November 2017
Received in revised form
13 February 2018
Accepted 19 February 2018

Keywords:
ZnO
Nanorods
Nanosheets
Growth mechanism
Dye-sensitized solar cell

ABSTRACT

Surfactant-free, ultrasound assisted modified successive ionic layer adsorption and reaction (M-SILAR) method and home-made microcontroller based low-cost potentiostat system are employed to prepare zinc oxide (ZnO) nanostructure based thin films. The comparison between physicochemical as well as photoelectrochemical (PEC) properties of the nanostructures prepared via two different template free, simplistic and cost-effective green routes have been discussed in detail. X-ray diffraction and Raman analysis confirm the formation of phase pure ZnO with the hexagonal crystal structure. Surface morphology significantly affects the physicochemical as well as PEC properties of ZnO thin films. Nanorods (NRs) and nanosheets (NSs) based ZnO thin films sensitized with N3 dye have been directly used as photoelectrodes in the dye-sensitized solar cell (DSSC). The power conversion efficiency (PCE) of 0.59% is achieved with J_{sc} of 4.04 mA/cm^2 and V_{oc} of 0.44 V for the DSSC in which the M-SILAR deposited 1-D ZnO NRs based thin film is used as the photoanode. While relatively less PCE of 0.29% with J_{sc} of 2.53 mA/cm^2 and V_{oc} of 0.36 V is obtained for DSSC prepared using electrodeposited 2-D ZnO NSs. In the NSs like 2-D surface morphology, the presence of multiple grain boundaries are acted as traps for the diffusing electrons, which reduces the electron mobility through it.

1. Introduction

To get rid of chemically hazardous and rare earth ingredients, third generation solar cells have been designed. They possess a great potential using nanomaterials and have gained a great breakthrough since Gratzel put forward the concept of a dye-sensitized solar cell (DSSC) [1]. In the past two decades, a large number of binary metal oxides such as TiO_2, ZnO, SnO_2, WO_3 and Nb_2O_5 have been tested as photoelectrode materials in the DSSCs [2–6]. Until now using TiO_2 as the DSSC photoanode, the power conversion efficiency (PCE) of more than 9% has been achieved with ruthenium-based N3 sensitizer [7]. Moreover, the 13% PCE has been achieved with porphyrin sensitizers using TiO_2 as a photoanode [8]. Up to now record PCE of 8.03% have been achieved with ZnO based DSSCs [9], which is much lower than that of TiO_2-based DSSC, still ZnO is regarded as a potential substitute for TiO_2 photoelectrode because of its similar electron affinity, wide band gap of 3.4 eV and exciting binding energy level (60 meV) with stable wurtzite structure [4]. Also, it possesses higher bulk mobility (100 cm^2/V^{-1}s^{-1}) indicating lower charge recombination [10]. Numerous kinds of ZnO nanostructures, particularly, one-dimensional (1-D) nanowires (NWs) or nanorods (NRs), and two-dimensional (2-D) nanosheets (NSs) or nanoplates (NPs) have been synthesized using the various physical and chemical methods including pulsed laser deposition (PLD), spray pyrolysis technique (SPT), hydrothermal method, chemical bath deposition (CBD), successive ionic layer adsorption and reaction (SILAR) and electrodeposition (ED) method [11–16]. In comparison, the PLD and SPT methods require high temperature with rigorous and complex conditions for the operation. From the technological point of view, SILAR and ED method offers much more inexpensive experimental setup, a rapid and economical method for preparation of large-area ZnO nanostructures with low-temperature processing, arbitrary substrate shapes, and offer precise control of film parameters [17,18]. Using the SILAR method, the thickness, composition and phase purity of thin films can be easily controlled just by regulating the growth parameters such as

---

* Corresponding author.
E-mail address: avm_phy@unishivaji.ac.in (A.V. Moholkar).

https://doi.org/10.1016/j.optmat.2018.02.040
0925-3467/

adsorption and reaction time, deposition cycles and precursor concentration [19–21]. Additionally, the deposition electrolyte of ED method can be reused, while the deposition solutions for other methods could be used only once.

In the DSSC, photoelectrode made up of wide band gap semiconducting material acts as the heart of the DSSC. Researchers are trying to improve the electron transport properties of the material by changing the morphology of the samples, such as 1 dimensional (1-D) nanowires (NWs), NRs or nanotubes (NTs), as every possible point of electron injection is directly connected to the substrate with a minimum number of interfaces and grain boundaries in between, which further improves the charge transport in the device [19]. 1-D ZnO nanostructures afford a direct conduction pathway for the photogenerated electrons, which is favorable for rapid electron transport in photoelectrode with reduced recombination loss [20]. The 2-D nanostructure of ZnO like NSs has also attracted much interest because of their unique advantages, such as the large surface area for the adsorption of sensitizers and enhanced light scattering capacity, which especially beneficial for applications in photoelectrochemical (PEC) cells [22].

Çakar et al. synthesized the ZnO plates, rods and nanoparticles using microwave assisted hydrothermal method and achieved 1, 0.83 and 0.41% power conversion efficiency for the respective samples with Fe-tannic acid complex dye as photosensitizer [23]. Marimuthu et al. prepared seed layer assisted ZnO nanorods as photoelectrode by ED method and obtained 3.75% PCE with Ru based N719 dye [24]. Using hydrothermal and dip-coating methods, Feng et al. prepared the ZnO/TiO_2 composite NRs for DSSC application. The top ZnO NRs facilitated large surface area for dye adsorption and TiO_2 NRs provided a direct pathway to the photogenerated electrons which results in a PCE of 4.36% [25]. Patil et al. have achieved the PCE of 2.9% by photonic sintering of a ZnO nanosheet based photoanode prepared by using solid-state synthesis with flash white light combined with deep UV irradiation [26]. Hedgehog-like hierarchical ZnO needle-clusters developed by Qu et al. by hydrothermal synthesis provides the high surface area for dye adsorption and also avoids extensive grain boundary formation which results in 2.2% PCE of the DSSC [27].

The limiting and time-consuming factor for traditional SILAR method is the slow growth rate. With the use of ultrasound-assisted M-SILAR method, nanostructured photo-electrodes can be directly prepared with less deposition time. The ultrasound works on the principle of the acoustic cavitation effect. The deposition rate and the film quality are expected to increase with the modification in the deposition process of ZnO nanostructure by the cavitation effect. Therefore, M-SILAR method has been used for the deposition of the nanostructured ZnO photo-electrodes to be used in DSSC's [28]. For ED, the microcontroller based low-cost potentiostat has been designed and developed. In the extensive literature survey, there are fewer reports on the synthesis of DSSC photoelectrodes by employing the simplistic M-SILAR and Electrodeposition green routes. So, in the present investigation, surfactant-free 1-D ZnO NRs have been grown without prior seed layer by changing the M-SILAR cycles and 2-D ZnO NSs have been deposited by employing ED method with variation in the deposition time. The probable growth mechanism processes of these nanostructures are also discussed. The comparison between physicochemical as well as PEC performance of ZnO nanostructures prepared by two different green routes is also debated in the present study.

2. Experimental

2.1. Preparation of ZnO thin films by M-SILAR method

ZnO thin films have been deposited using zinc-ammonia complexed precursor ($Zn(NH_3)_n^{2+}$) as cationic source and 1% diluted hydrogen peroxide (H_2O_2) kept at 353 K temperature as an anionic source with slight modifications as discussed in our previous report [29]. The schematic setup used for M-SILAR deposition of ZnO thin films is as shown in Fig. 1 (A). The M-SILAR cycles have been repeated successively for 50, 100, 150 and 200 times and the as-deposited films were annealed at 673 K in an air for 1 h to remove the hydroxide phase and to increase the crystallinity. The films are denoted as SZ-5, SZ-10, SZ-15 and SZ-20 samples for 50, 100, 150 and 200 deposition cycles, respectively and these samples were further used for their structural and morphological studies.

2.2. Preparation of ZnO thin films by ED method

In this study, Atmel AT89C51 microcontroller is used to generate basic electrical output such as constant current, constant voltage, and forward and reverse pulse with pulse width modulation (PWM) capabilities. The total cost of the system nearly equals to 50 USD. A typical block diagram of the proposed system is shown in Fig. 1 (B). The microcontroller can produce 0–5000 mV voltage with the help of 8 bit digital to analog converter DAC0808 (Texas Instruments). The operational amplifier (Op-Amp) circuits are responsible for the precise control of constant voltage, constant current, and forward and reverse pulse with pulse width modulation (PWM). The constant current is generated using Op-Amp and Zener diode circuit, whereas the PWM is achieved by conventional triangle-wave generator circuits. The software code of the present system is written in the Keil integrated development environment (IDE). ED of ZnO thin films was performed with the microcontroller based potentiostat in a standard three electrodes system. The block diagram of microcontroller based potentiostat used for the ED of ZnO NSs is as shown in Fig. 1 (B). Graphite and saturated calomel electrode (SCE) are used as the counter electrode and the reference electrode, respectively. The flexible stainless steel (SS) and fluorine doped tin oxide (FTO) substrates were used as working electrode. The electrolyte was 0.05 M $Zn(NO_3)_2$ aqueous solution and 0.1 M KCl was introduced into it as a supporting electrolyte. ZnO thin films were obtained by potentiostatic electrodeposition at -1.0 V (versus SCE) at the constant temperature of 80 °C by varying deposition time for 5, 10, 20 and 30 min. The as-deposited films were annealed at 673 K in an air for 1 h to remove the hydroxide phase included if any. The films are denoted as EZ-5, EZ-10, EZ-20 and EZ-30 samples for 5, 10, 20 and 30 min deposition time, respectively.

2.3. Assembly of ZnO-based DSSCs

The optimized M-SILAR and electrodeposited ZnO samples have been soaked in ethanolic 0.3 mM *cis*-Bis (isothiocyanato) bis(2,2′-bipyridyl-4,4′-dicarboxylato ruthenium) (II) i.e. N3 dye solution at room temperature for 12 h and then washed cautiously in ethanol, afterward the dye-loaded films have been dipped in acetonitrile and dried up in an air. Compact DSSCs have been fabricated using a typical two electrode configuration with an active area of 0.25 cm^2. Dye-loaded ZnO samples have been used as photoelectrode and platinum (Pt) coated FTO as the counter electrode. The predrilled FTO substrates were ultrasonically washed and the Pt counter electrode is prepared by drop cast method using the 10 mM hexachloroplatinic acid ($H_2PtCl_6 \cdot 6H_2O$) in 2-propanol solution with annealing at 450 °C for 10 min. The two electrodes have been assembled using the thermoplastic (1 mm). The space between the electrodes is filled with an electrolyte comprising of 0.1 M lithium iodide and 0.05 M iodine in acetonitrile through the predrilled hole in the counter electrode.

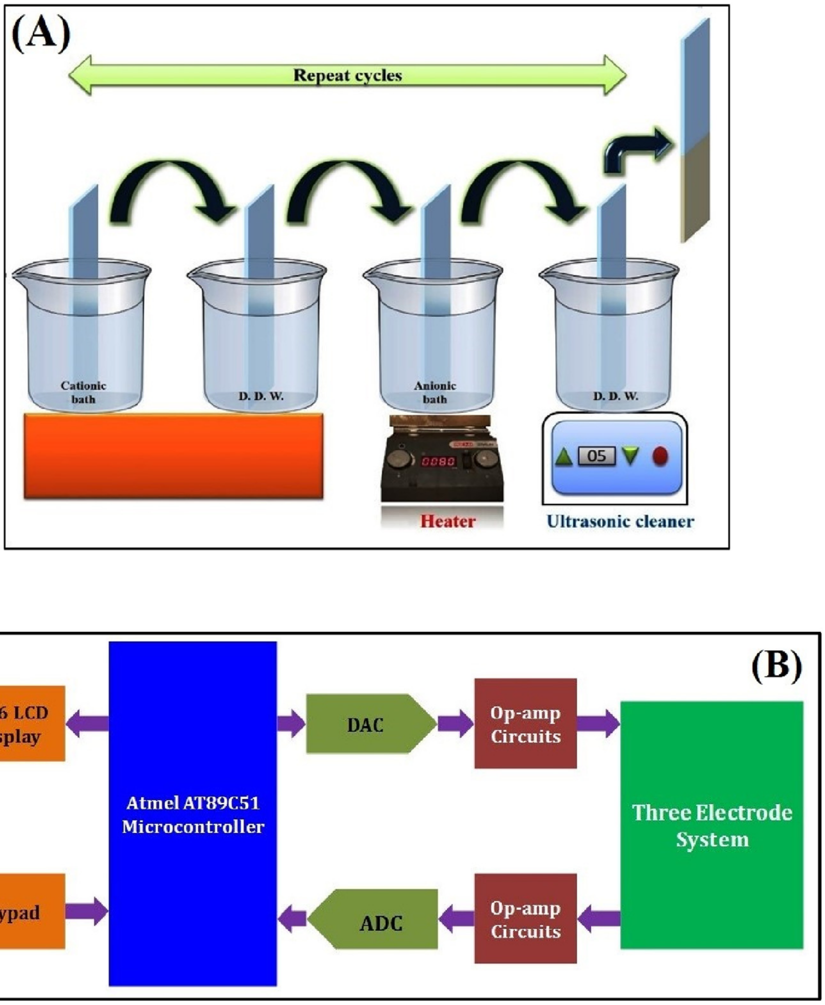

Fig. 1. Schematic setup of (A) M-SILAR method and (B) Block diagram of microcontroller based potentiostat used for electrodeposition of ZnO thin films.

2.4. Characterization techniques

The structural properties of M-SILAR and electrodeposited ZnO samples have been studied using X-ray diffractometer (XRD) (Philips, PW 3710, Holland) operated at 40 kV, 30 mA with Cu K_α radiation ($\lambda = 1.54$ Å). The thickness measurement is accomplished with the help of XP-I stylus surface profiler (AMBIOS, USA). Raman spectra are recorded using the Raman microscope (LabRam, HR800 UV-Raman microscope (Horiba Jobin-Yvon, France), KBSI, Gwangju-center, South Korea) with the excitation wavelength of 514 nm using diode laser. The surface morphology is observed by means of scanning electron microscopy (SEM) (JEOL JSM -6360, Japan). The elemental composition of the deposited material is examined by energy dispersive X-ray spectrometer (EDAX) (Bruker, nano GmbH, Germany, attached to the FE-SEM). UV–visible absorbance spectra of the samples have been obtained by means of a UV–visible spectrophotometer (UV1800, Shimadzu, Japan). J-V curves have been recorded on the solar simulator (model CT- 150 AAA, photoemission tech, USA) under an Air Mass 1.5 G solar irradiation. Electrochemical impedance study is carried out with the electrochemical workstation (AUT85804, Netherlands) using the frequency range of 1 MHz to 0.1 Hz in AC mode (100 mV). The same devices assembled for checking PEC performance have been used for electrochemical impedance study.

3. Results and discussion

3.1. X-ray diffraction study

Fig. 2 (A) shows the XRD patterns of SZ-5, SZ-10, SZ-15 and SZ-20 samples prepared with different M-SILAR deposition cycles. All the diffraction peaks are indexed to a hexagonal wurtzite structure of ZnO, which agrees well with the standard JCPDS Card No. 00-003-0888. The XRD patterns of all the samples are dominated by strong (002) diffraction peak, which suggests that the ZnO nanostructure is favorably oriented along c axis [30]. The intensity of (002) peak increases with increasing deposition cycles i.e. thickness of the sample. Initially, for SZ-5 sample, the film thickness is found to be 1.10 μm which further increased to 1.22 μm for SZ-10 sample. The intensity of (002) plane is observed highest for the SZ-15 sample which has a thickness of 1.92 μm. The growth of the c-axis direction suppressed and intensity of (002) peak decreases for SZ-20 sample, due to the overgrowth and peel off process of the film, which leads to decrease in thickness to 1.45 μm [15]. Fig. 2 (B) displays the XRD patterns of the ZnO samples deposited with the ED method. Since the samples have been deposited on the SS substrate, several characteristic signals of the substrate denoted by asterisks (*) have been appeared in all the spectra [31]. Other observed peaks are attributed to the diffractions from (100), (002) and (101) planes respectively, which can be indexed to the

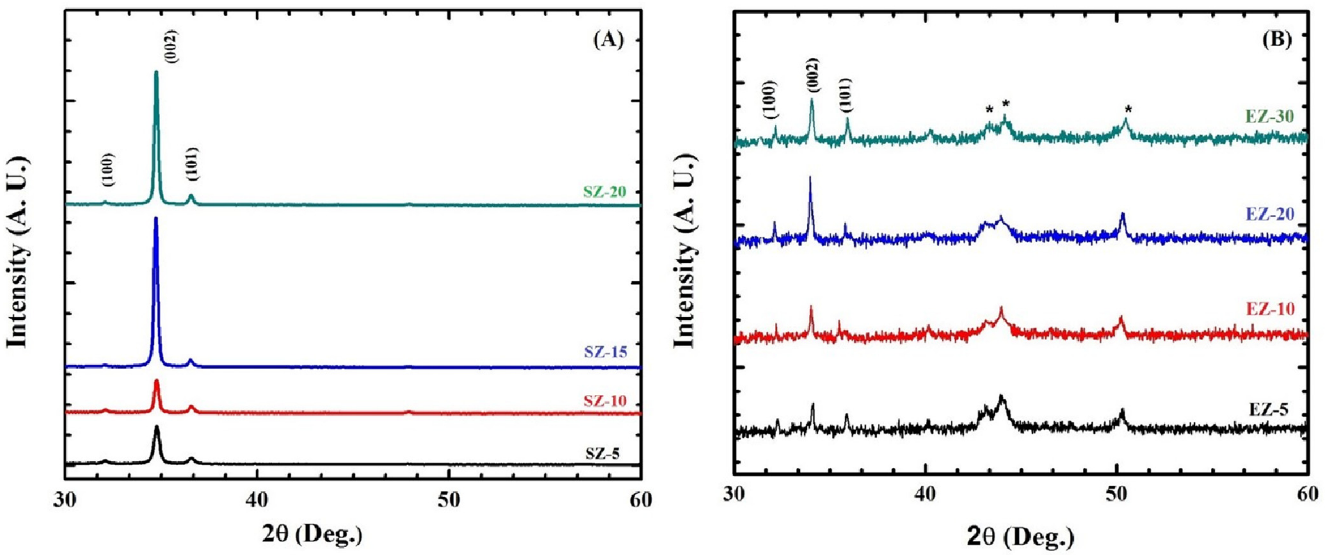

Fig. 2. XRD patterns of (A) M-SILAR deposited SZ-5, SZ-10, SZ-15, SZ-20 samples prepared with varying M-SILAR cycles and (B) electrodeposited EZ-5, EZ-10, EZ-20 and EZ-30 samples prepared with varying deposition time.

hexagonal wurtzite structure of ZnO in agreement with the data obtained from JCPD card No. 00-005-0664, indicating the good crystallization of electrodeposited ZnO. From the thickness measurement study, the sample EZ-5 has a thickness of 0.35 μm, which increases further to 0.42 μm for EZ-10 sample, with the increase in deposition time. The maximum peak intensity (002) is observed for the sample EZ-20 which has thickness 0.67 μm. Further, increase in the deposition time for sample EZ-30 results in the overgrowth and peel off of the film with a reduced thickness of 0.58 μm, which is responsible for the decrease in peak intensity as shown in Fig. 2 (B).

3.2. Morphological study

3.2.1. Scanning electron microscopy (SEM)

Fig. 3(a–d) shows the SEM images of M-SILAR deposited SZ-5, SZ-10, SZ-15 and SZ-20 samples. The significant effect of variation of M-SILAR cycles on the nanostructure and thickness of the samples is clearly observed. The growth of the nuclei on the substrate occurs by diffusion of clusters and coalescence of these clusters gives rise to the formation of a uniform thin film [32]. In sample SZ-5, several voids are seen with the heterogeneous distribution of unevenly shaped grains. The grains are not well interconnected to each other (Fig. 3 a). For 100 cycles, bigger grains are obtained with more compactness and having an almost same diameter. The black spots represent the voids, means nucleation centers are absent. Relatively fewer voids are observed for SZ-10 sample (Fig. 3 b). Well growth of compact and unique structure is observed for SZ-15 sample (Fig. 3 c). The surface of the substrate is well covered by resultant uniform NRs like structure. The diameter of rod increases as M-SILAR cycles increases. For SZ-15 sample, the resultant NRs are observed to be grown perpendicular to the substrate surface and are densely covered over the substrate. For the SZ-20 sample, the disorder increases and randomly oriented NRs are observed. This supports well to the XRD results as discussed in

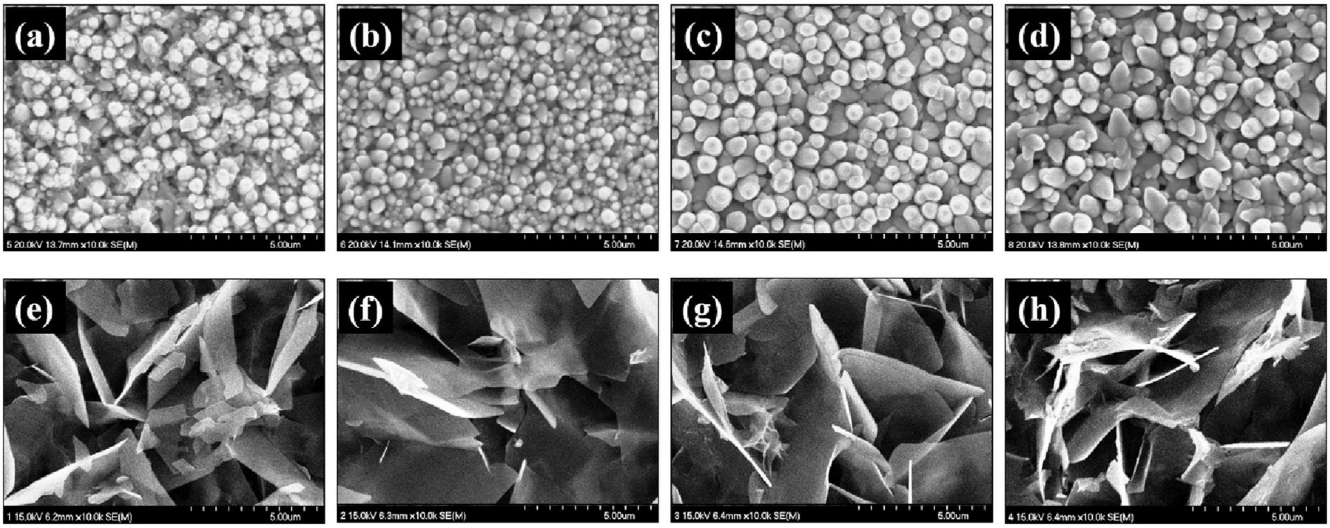

Fig. 3. SEM images of M-SILAR deposited (a) SZ-5, (b) SZ-10, (c) SZ-15, (d) SZ-20 prepared with varying M-SILAR cycles and electrodeposited (e) EZ-5, (f) EZ-10, (g) EZ-20 and (h) EZ-30 samples prepared with varying deposition time, respectively.

earlier section.

Fig. 3(e–h) depicts the SEM images of the electrodeposited ZnO samples. In Fig. 3(e), for 5 min deposition time, randomly oriented NSs are developed, however, for the reaction time, 10 min, the improved surface morphology of NSs have been observed. For EZ-20 sample, the arrangement of fine interconnected vertical free-standing NSs with triangular geometry is clearly seen. Width and thickness of the sheets are in the ranges of 4–5 μm and 50–70 nm, respectively. Further for EZ-30 sample, NSs seems to be damaging may be due to the overgrowth of the sample, which correlates well with the XRD study.

From the structural and surface morphological analysis, it is considered that the M-SILAR deposited SZ-15 and electrodeposited EZ-20 samples are found to be optimum as they show better crystallinity and well-defined nanostructures than any other samples. Thus, these SZ-15 and EZ-20 samples have been further characterized for their compositional, optical, surface wettability, PEC and EIS studies.

3.2.2. *Possible growth mechanism of ZnO NRs via M-SILAR and NSs via ED method*

On the basis of the observed SEM results, one can predict the growth mechanism of highly c-axis-oriented and arbitrarily grown ZnO NRs and NSs as shown in Fig. 4 (A and B). Basically, the evolution of obtained NRs depends on the nucleation and growth processes. In the M-SILAR method, the forces responsible for making the desired ZnO films may be cohesive forces or Van-der-Waals forces or chemical attractive forces [33]. With the increase in M-SILAR cycles, the growth of the particles occurs on earlier grown nuclei. The possible growth mechanism of ZnO NRs is depicted in Fig. 4 (A). The ZnO thin film grow along (002) plane because, ZnO has positively charged (0001) and negatively charged (000-1) polar surfaces, thus, the nature of the ZnO crystals becomes polar, and the Zn-rich positive (0001) surface being more reactive and more stable due to relatively low surface energy than the oxygen-rich negative (000-1) facet [34]. According to the lowest energy principle, hexagonal ZnO crystals grow along the [0001] direction to achieve the surface energy minimization by attracting new opposite ionic species to its surface to promote anisotropic growth along the [0001] direction. Thus along the c-axis direction, the growth rate is far faster than along any other crystallographic directions, which lead to the formation of 1-D NRs like structure of ZnO [35].

During the ED process, Zn $(NO_3)_2$ firstly changes into Zn^{2+} with the acid solution, according to Eq. (1). The reaction of ions NO_3^-, H_2O, and $2e^-$ gives rise to the formation of OH^- in Eq. (2). Under the influence of electrostatic interactions, the formed Zn^{2+} ions have a tendency to adsorb on the SS/FTO substrate and the active nucleation sites are almost generated on the surface of a substrate, which is beneficial to the subsequent growth of ZnO on the substrates. Then, hydroxylation reaction between OH^- ions and Zn^{2+} ions would rapidly occur on the surface of the electrode to form $Zn(OH)_2$ (Eq. (3)). Then, $Zn(OH)_2$ would readily decompose into ZnO if the solution temperature is 80 °C (Eq. (4)) [36].

$$Zn\ (NO_3)_2 \rightarrow Zn^{2+} + 2NO_3^- \tag{1}$$

$$NO_3^- + H_2O + 2e^- \rightarrow NO_2^- + 2OH^- \tag{2}$$

$$Zn^{2+} + 2OH^- \rightarrow Zn(OH)_2 \tag{3}$$

$$Zn(OH)_2 \rightarrow ZnO + H_2O \tag{4}$$

In the growth progression, firstly, ZnO seed layer as the lattice-matched template is formed during the above controlled nucleation and growth process and the growth rate ratio of c-axis direction to other crystallographic directions reduces greatly due to the shielding effect of OH^- ions on the (0001) surface which results in the formation of ZnO nanosheets [37]. On the other hand, the presence of appropriate capping agents like Cl^-, tend to preferentially adsorb onto the positively charged (0001) planes, subsequently, to hamper the crystal growth along the c-axis, resulting in the development of ZnO NSs [38].

3.3. *Raman spectroscopy*

Fig. 5 shows the Raman spectra of the optimized SZ-15 and EZ-20 samples. Foremost peaks at 100 cm^{-1} and 438 cm^{-1} are

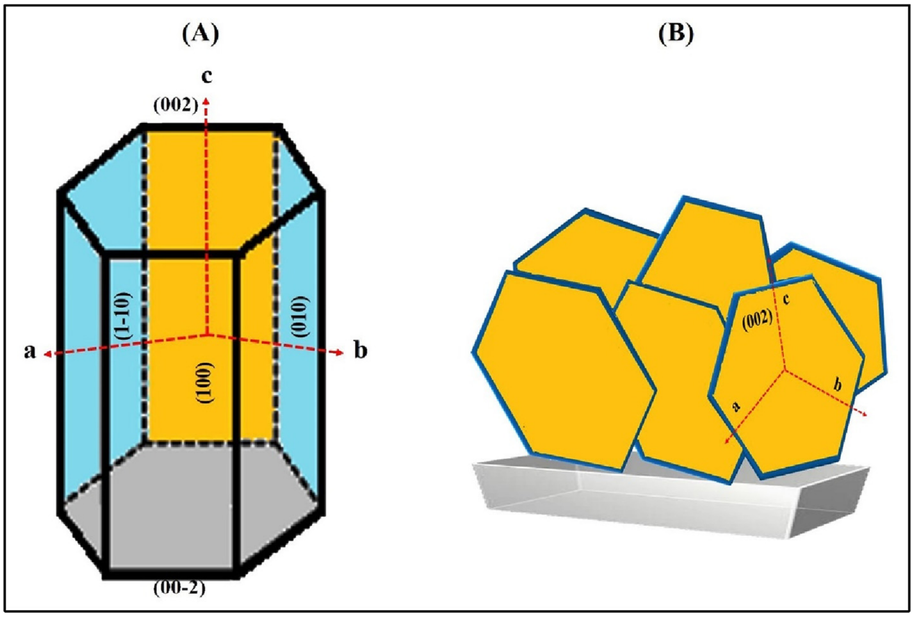

Fig. 4. Schematics showing the growth mechanisms of (A) M-SILAR deposited ZnO nanorods and (B) electrodeposited ZnO nanosheets.

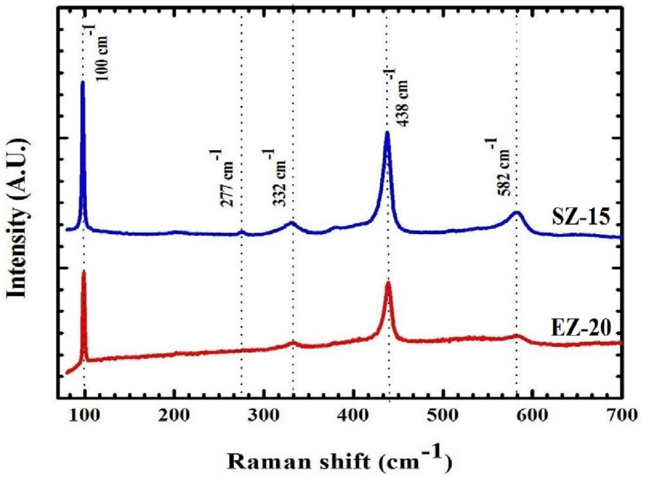

Fig. 5. Raman spectra of typically optimized SZ-15 and EZ-20 samples, deposited by M-SILAR and ED methods, respectively.

identified which are related to the vibrations of the heavy Zn sublattice and the oxygen atom, respectively and these peaks are assigned to Raman active low-E_2 and high-E_2 mode of nonpolar optical phonons. The peak at 277 cm^{-1} (B_1 low) belongs to the silent mode of w-ZnO. The weaker peak at 332 cm^{-1} has been attributed to a second-order nonpolar E_2 mode, arising from zone boundary phonons [39]. The peak observed at 582 cm^{-1} is associated with the defects such as oxygen vacancy or interstitial zinc in ZnO. Thus, the observed peaks strongly support the XRD analysis concerning the formation of w-ZnO [40].

3.4. *EDAX study*

Fig. 6 shows the EDAX spectra of (a) optimized SZ-15 and (b) EZ-20 samples, respectively. The Zn and O signals have been detected, which indicated that the nanostructures are made up of Zn and O. The atomic percentage ratio of Zn to O is found to be 1.12 and 0.75 for the SZ-20 and EZ-20 samples, respectively, which confirms the samples are nearly stoichiometric in the composition. Slightly increased oxygen content is observed for EZ-20 sample may be due to the chemisorption of oxygen during the annealing process of the sample.

3.5. *Optical study*

Fig. 7 (A) shows the absorbance versus wavelength spectra of SZ-15 and EZ-20 samples, without dye loading. The spectra revealed that the ZnO samples have a low absorbance in the visible region, due to its wide band gap energy. The absorption data is analyzed and the band gap values (E_g) are estimated using classical relationship amongst the absorption coefficient (α) and the photon energy ($h\nu$) using the relation $(\alpha h\nu)^2 = h\nu - E_g$ Ref. [41]. The E_g values are found to be 3.11 eV and 3.19 eV for SZ-15 and EZ-20 samples, respectively (Fig. 7 B). The difference between these values is due to the variation in the thickness of the samples prepared by two different methods [42].

To study the effect of dye loading on the absorption of the ZnO samples, optical absorption spectra have been recorded. Fig. 7 (C) shows the absorption spectra of N3 dye-loaded SZ-15 and EZ-20 samples. The maximum absorption peak around 500 nm is seen with broader coverage in the visible region of the solar spectrum after dye-loading which is corresponding to the visible $t_2 \rightarrow \pi^*$ metal-to-ligand charge transfer (MLCT) in N3 dye, which is in good agreement with the previous report [43]. SZ-15 sample shows stronger absorption than that of EZ-20 sample, which can be attributed to better dye loading due to well-aligned NRs as depicted in SEM studies (Fig. 3 c).

3.6. *Surface wettability study*

Surface wettability involves the interaction between a liquid and a solid in contact which is an important parameter in surface science and its measurement provides a simple and reliable method for the understanding of surface engineering. The surface wettability study is used as a diagnostic method to determine the quality of deposited metal chalcogenide/oxide thin film absorbers without performing actual application [44]. As the surface tension reflects the surface energy, which is directly associated with the chemical nature of the surface. From Fig. 8, the electrolyte contact angles for samples SZ-15 and EZ-20 are observed as 28^0 and 15^0, respectively. EZ-20 sample shows less contact angle than that of SZ-15 may be due to the more rough surface morphology of the sample. These values indicate hydrophilic nature of ZnO samples as contact angle is less than 90^0. The hydrophilic nature supports the percolation of the electrolyte through the pores of the material facilitating the ionic conduction for improving the performance of thin film solar cells [45].

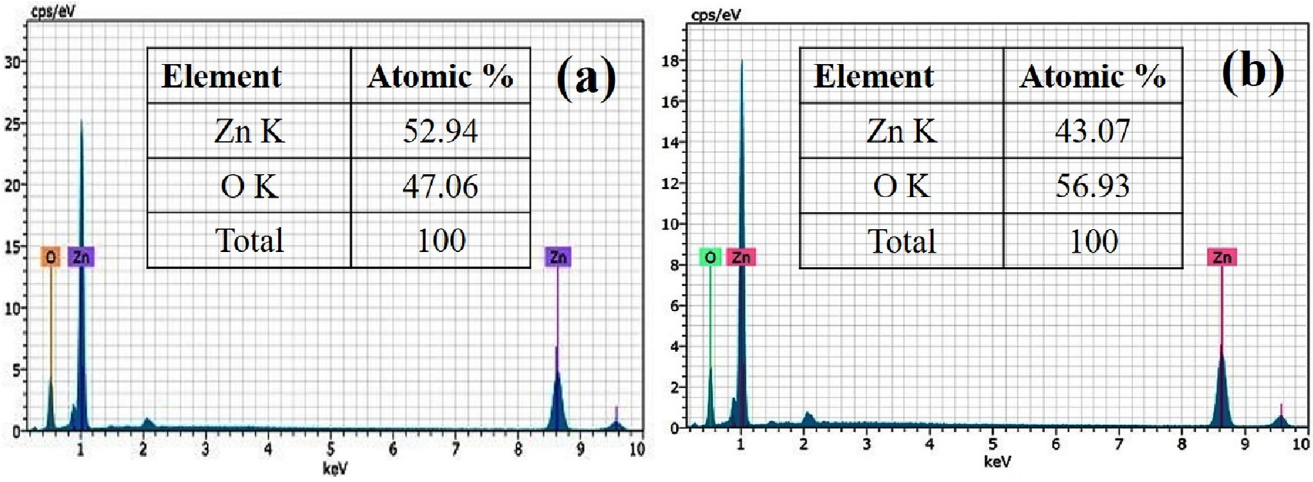

Fig. 6. EDAX spectra of typically optimized SZ-15 and EZ-20 samples prepared via M-SILAR and ED methods, respectively.

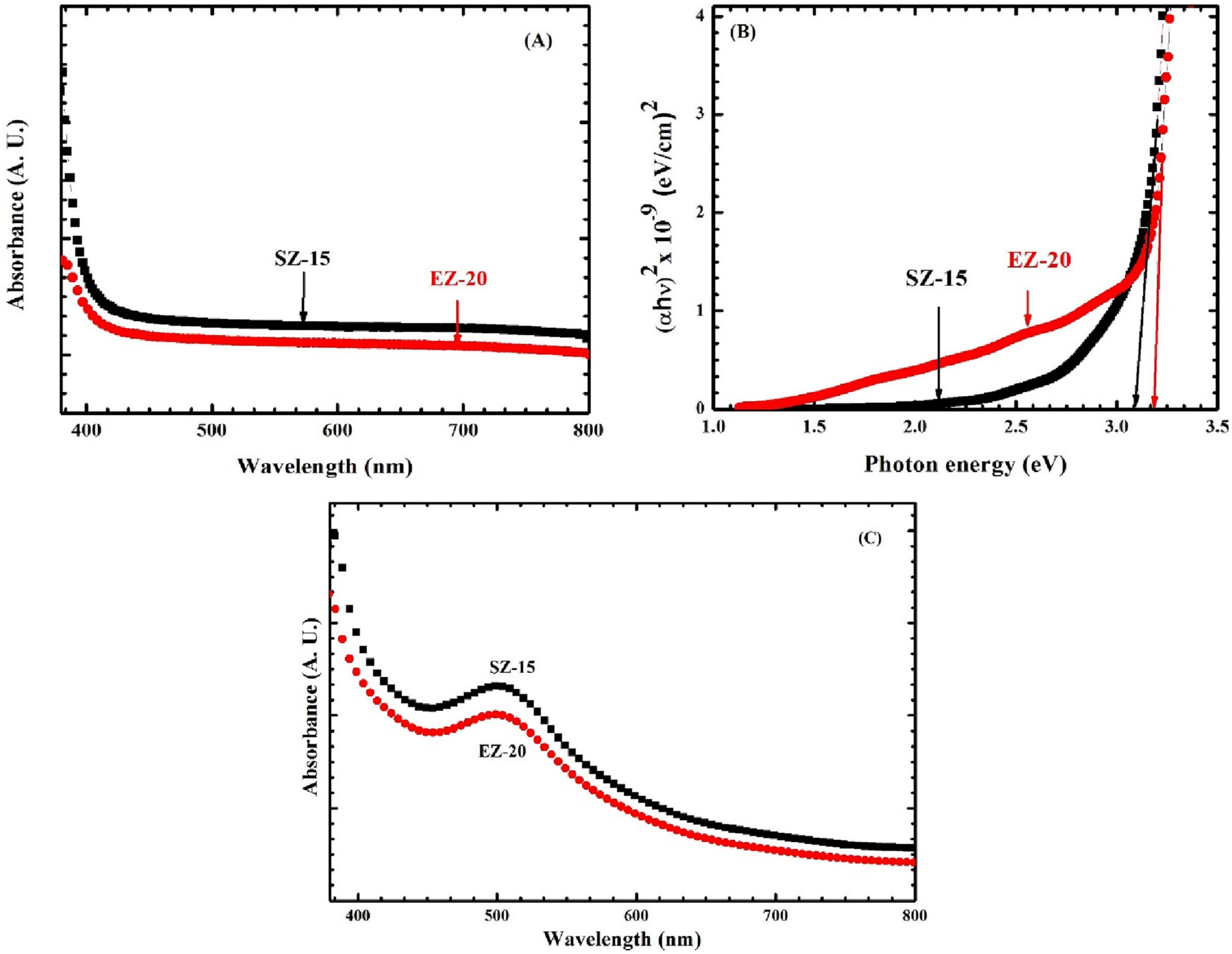

Fig. 7. (A) Absorbance Vs. wavelength spectra of bare optimized SZ-15 and EZ-20 samples, (B) Variation of $(\alpha h\nu)^2$ versus photon energy for the estimation of optical band gap energy of the optimized SZ-15 and EZ-20 samples without dye-loading and (C) Absorbance Vs. wavelength spectra of N3 dye-loaded SZ-15 and EZ-20 samples deposited via M-SILAR and ED method, respectively.

3.7. J-V measurement

Fig. 9 (A) shows the ideal diode behavior due to the formation of a junction between the ZnO photoelectrodes and electrolyte. Fig. 9 (B) shows the photocurrent density versus voltage (J-V) curves under illumination of DSSCs prepared using optimized SZ-15 and EZ-20 samples, respectively. Table 1 shows the several solar cell parameters for the DSSCs, where J_{sc} is the short circuit current density, V_{oc} is the open-circuit voltage, FF is the fill factor, η is the PCE, R_s is the series resistance and R_{sh} is the shunt resistance. DSSC prepared using SZ-15 sample exhibited the highest PCE of 0.59%, with its maximum J_{sc} of 4.04 mA/cm^2 and V_{oc} of 0.44 V. This device contributes highest PCE due to well-defined 1-D nanostructure (Fig. 3 (c)), which allows enhanced internal surface area for dye adsorption and facilitates direct pathway for faster electron transport by reducing charge recombination rate through it [46]. The chemical stability is found to be the main issue for ZnO photoelectrode. The low PCE of ZnO-based DSSC is a consequence of dye aggregation effect. The longer dye adsorption time gives rise to Zn^{2+} -dye aggregates on the surface of the photoelectrode due to acidic nature of the dye. This result in an etching of the ZnO surface due to which the nanostructure of ZnO gets totally damaged. The highly gathered dye aggregates are mainly responsible for low FF and reduction in the potential between ZnO photoelectrode and counter electrode [47]. DSSC based on EZ-20 sample showed relatively less PCE of 0.29% with J_{sc} of 2.53 mA/cm^2 and V_{oc} of 0.36 V compared to that of DSSC based on SZ-15 sample. This could be due

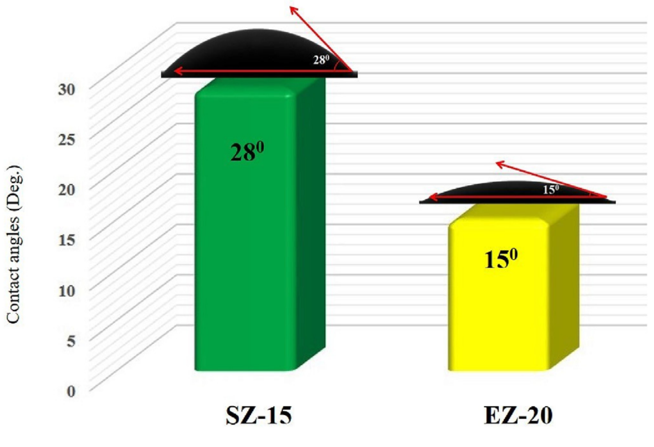

Fig. 8. Electrolyte contact angle images of the SZ-15 and EZ-20 samples deposited via M-SILAR and ED method, respectively.

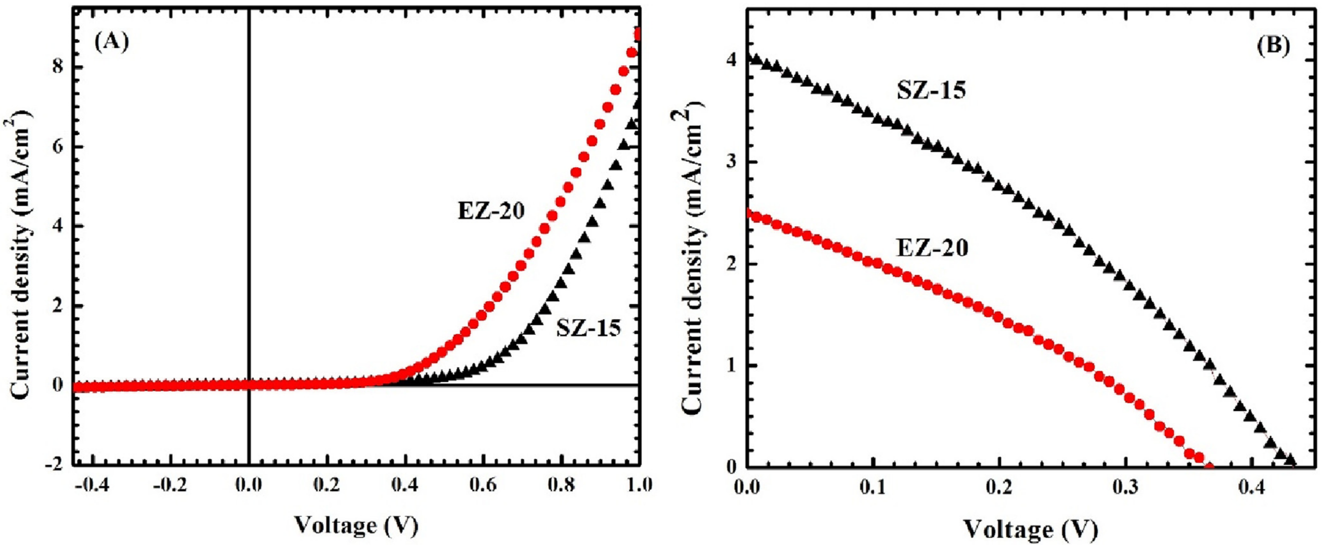

Fig. 9. Photocurrent density-voltage (J–V) curves (A) under dark (B) upon illumination for DSSCs prepared using SZ-15 and EZ-20 samples deposited via M-SILAR and ED method, respectively.

Table 1
Photoelectrochemical performance and electron transport properties of the DSSCs prepared using M-SILAR deposited optimized SZ-15 and electrodeposited EZ-20 samples determined by photocurrent density-voltage (J-V) characteristics and electrochemical impedance spectroscopy (EIS) analysis, respectively.

DSSC	Thickness (μm)	Solar cell parameters						EIS parameters			
		J_{sc} (mA/cm^2)	V_{oc} (V)	FF	η (%)	R_s (Ω)	R_{sh} (Ω)	R_s (Ω)	R_1 (Ω)	R_2 (Ω)	τ_e (μs)
SZ-15	1.92	4.04	0.44	0.33	0.59	260	980	33.2	66.8	97.1	150
EZ-20	0.67	2.53	0.36	0.32	0.29	320	435	36.8	150	178	42

to the presence of multiple grain boundaries which acts as traps for the diffusing photogenerated electrons in the NSs like 2-D surface morphology, which reduces the electron mobility through it.

Liu et al. [48] reported the synthesis of ZnO NWs by microwave heating method with prior seed layer using pulsed laser deposition (PLD) technique. They achieved the maximum PCE of 1.25% with J_{sc} of 6 mA/cm^2, V_{oc} of 0.58 V and FF of 0.36 for ZnO NWs based DSSC. Singh et al. [49] have deposited silver doped ZnO films by the spin coating method and used as photoelectrode in DSSC with N719 dye and achieved 0.44% PCE with J_{sc} of 1.55 mA/cm^2, V_{oc} of 0.60 V and FF of 0.48. Jimenez-Cadena et al. have synthesized different ZnO nanostructures by physical vapor deposition (PVD) and attained highest power conversion efficiency of 0.51% with J_{sc} of 0.52 mA/cm^2, V_{oc} of 0.68 V and FF of 0.34 by using ZnO NWs based DSSC [50].

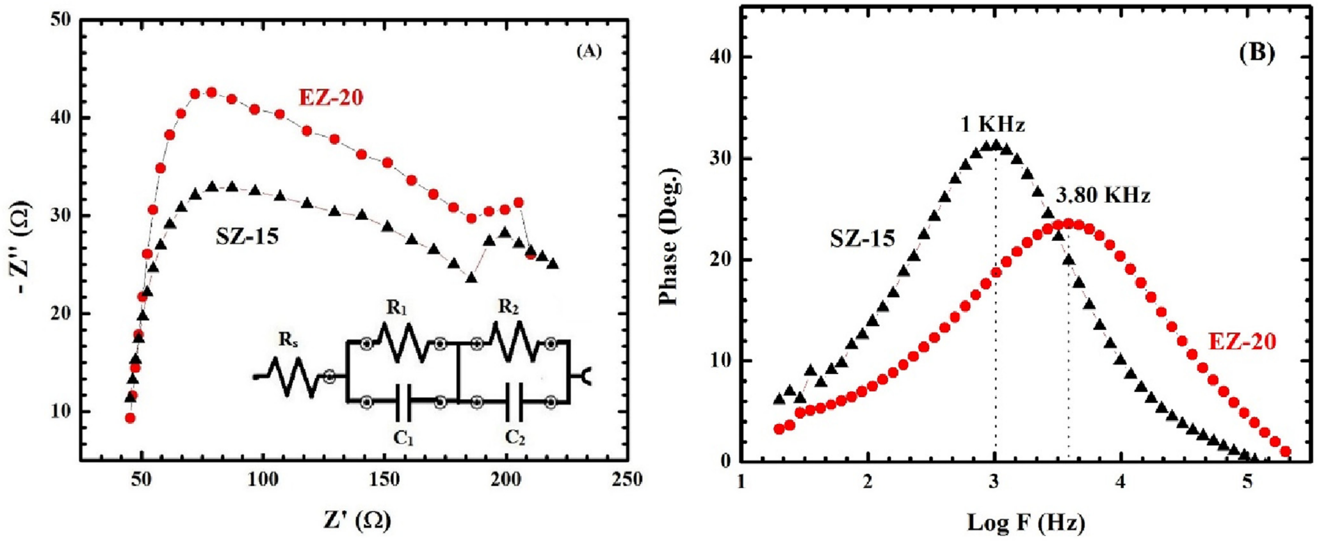

Fig. 10. (A) Nyquist plots, measured in the dark under 100 mV applied bias, inset shows equivalent circuit model used to analyze the EIS data and (B) Bode plots of DSSCs prepared using SZ-15 and EZ-20 samples deposited via M-SILAR and ED method, respectively.

However, above mentioned photoelectrode synthesis methods require sophisticated equipment, vacuum-based complicated experimental conditions, high working temperature and costly substrates. In present study, though the relatively less PCE is achieved but, the employed green chemical routes are facile and cost-effective. Also, no vacuum is needed at any stage of the experiment.

3.8. EIS study

The parameters related to charge recombination and electron transport properties of the respective ZnO photoelectrodes have been calculated by using the EIS study. The experimental impedance data, given by Nyquist plots in Fig. 10 (A) has been fitted to the equivalent circuit (inset of Fig. 10 (A)), where, R_1 and C_1 represent charge transfer behavior at counter electrode (Pt- FTO)/electrolyte interface, R_2 and C_2 assigned to charge transfer resistance at photoelectrode/electrolyte interface. R_s is the solution resistance [51]. From Table 1, it is seen that sample SZ-15 has $R_1 = 66.8\ \Omega/cm^2$ and $R_2 = 97.1\ \Omega/cm^2$, which are relatively much lower than that of EZ-20 sample. The likely reason for this lower charge transport resistance is the well-aligned 1D-NRs like structure of M-SILAR deposited ZnO sample which easily permits the axial charge transport with the low recombination [52]. This means, for SZ-15 sample more electrons are injected into the ZnO photoanode and undergo forward transport in the photoanode, which is in accordance with the increase in J_{sc} value [53]. In addition, electron life time (τ_e) is calculated using Bode plots (Fig. 10 (B)) by the formula, $\tau_e = 1/2\pi F_{max}$ [54], where, F_{max} is the characteristic frequency at the top of the arc. The SZ-15 sample has highest $\tau_e = 150\ \mu s$, as it possesses relatively superior 1-D nanostructure which provides the effective pathway to the photogenerated electrons with low recombination rate, leads to achieving the high PCE. Thus, the EIS analysis shows that ZnO NRs provide a direct pathway for accelerating electron transport, extending the electron lifetime, suppressing electron recombination and improving electron collection efficiency [55,56]. The sample EZ-20 shows inferior electron lifetime of 42 μs, may be due to the more recombination losses and nanostructure with large grain boundaries. Thus, the observed results are in good agreement with the J-V results.

4. Conclusions

A simplistic methodology to prepare ZnO NRs via M-SILAR method and ZnO NSs via microcontroller based low-cost potentiostat by means of ED method and their use as a photoelectrode in DSSCs has been demonstrated. The results by M-SILAR and ED method are compared on the basis of their morphology. The M-SILAR deposition gives rise to thin films composed of ZnO NRs, while ED results in the formation of ZnO NSs. The surface morphology of ZnO samples has a significant impact on their DSSC performance. DSSC prepared using ZnO NRs exhibited the highest PCE of 0.59%, with its maximum J_{sc} of 4.04 mA/cm^2 and V_{oc} of 0.44 V than that of NSs based DSSC which showed the relatively less PCE of 0.29% with J_{sc} of 2.53 mA/cm^2 and V_{oc} of 0.36 V. Enhanced PCE for the DSSCs composed of ZnO NRs can be straightly associated with the faster electron transport mechanism with longer photoinduced electron lifetime. The 2-D NSs allows the large surface area for N3 dye adsorption, but it reduces the electron mobility through it, due to the presence of multiple grain boundaries. M-SILAR deposited films are superior to electrodeposited films in terms of their physicochemical as well as PEC properties.

Acknowledgements

This work was supported by the DAE- BRNS, Mumbai, India, through major research project (No. 2013/36/29-BRNS/2351). The authors are thankful to Physics Instrumentation Facility Center (PIFC), Department of Physics, Shivaji University, Kolhapur, for the characterization facilities.

References

[1] B. O'Regan, M. Gratzel, Nature 353 (1991) 737–740.
[2] D. Zhong, Q. Jiang, B. Huang, W.H. Zhang, C. Li, J. Energy Chem. 24 (2015) 626–631.
[3] A. Yella, H.W. Lee, H.N. Tsao, C. Yi, A.K. Chandiran, M.K. Nazeeruddin, E.W.G. Diau, C.Y. Yeh, S.M. Zakeeruddin, M. Gratzel, Science 334 (2011) 629–634.
[4] N. Memarian, I. Concina, A. Braga, S.M. Rozati, A. Vomiero, G. Sberveglieri, Angew. Chem. 123 (2011) 12529–12533.
[5] A. Thapa, J. Zai, H. Elbohy, P. Poudel, N. Adhikari, X. Qian, Q. Qiao, Nano Res. 7.8 (2014) 1154–1163.
[6] T.S. Eom, K.H. Kim, C.W. Bark, H.W. Choi, Mol. Cryst. Liq. Cryst. 602.1 (2014) 81–87.
[7] X. Yan, L. Feng, J. Jia, X. Zhou, Y. Lin, J. Mater. Chem. A 1.17 (2013) 5347–5352.
[8] S. Mathew, A. Yella, P. Gao, R.H. Baker, B.F.E. Curchod, N.A. Astani, I. Tavernelli, U. Rothlisberger, M.K. Nazeeruddin, M. Gratzel, Nat. Chem. 6 (2014) 242–247.
[9] Y. He, J. Hu, Y. Xie, Chem. Commun. 51 (2015) 16229–16232.
[10] G.J. Chang, S.Y. Lin, J.J. Wu, Nanoscale 6.3 (2014) 1329–1334.
[11] L. Liu, K. Hong, X. Ge, D. Liu, M. Xu, J. Phys. Chem. C 118.29 (2014) 15551–15555.
[12] N.L. Tarwal, P.S. Patil, Electrochim. Acta 56 (2011) 6510–6516.
[13] K. Mahmood, H.W. Kang, S.B. Park, H.J. Sung, Appl. Mater. Interfaces 5.8 (2013) 3075–3084.
[14] E. Puyoo, G. Rey, E. Appert, V. Consonni, D. Bellet, J. Phys. Chem. C 116.34 (2012) 18117–18123.
[15] S.K. Shaikh, V.V. Ganbavle, S.I. Inamdar, K.Y. Rajpure, RSC Adv. 6.31 (2016) 25641–25650.
[16] A. Brayek, S. Chaguetmi, M. Ghoul, I. Ben Assaker, A. Souissi, L. Mouton, P. Beaunier, S. Nowak, F. Mammeri, R. Chtourou, S. Ammar, RSC Adv. 6.37 (2016) 30919–30927.
[17] I. Şişman, M. Can, B. Ergezena, M. Biçer, RSC Adv. 5.90 (2015) 73692–73698.
[18] M.P. Suryawanshi, P.S. Patil, S.W. Shin, K.V. Gurav, G.L. Agawane, M.G. Gang, J.H. Kim, A.V. Moholkar, RSC Adv. 4 (2014) 18537–18540.
[19] J.B. Baxter, E.S. Aydil, Sol. Energy Mater. Sol. Cells 90.5 (2006) 607–622.
[20] B. Weintraub, Z. Zhou, Y. Li, Y. Deng, Nanoscale 2.9 (2010) 1573–1587.
[21] A.I. Inamdar, S.H. Mujawar, V. Ganesan, P.S. Patil, Nanotechnology 19 (2008) 325706–325712.
[22] J. Qiu, M. Guo, X. Wang, Appl. Mater. Interfaces 3 (2011) 2358–2367.
[23] S. Çakar, M. Ozacar, Spectrochim. Acta A 163 (2016) 79–88.
[24] T. Marimuthu, N. Anandhan, R. Thangamuthu, Appl. Surf. Sci. 428 (2018) 385–394.
[25] Y. Feng, J. Chen, X. Huang, W. Liu, Y. Zhu, W. Qin, X. Mo, Cryst. Res. Technol. 51 (2016) 548–553.
[26] S.A. Patil, H.J. Hwang, M.H. Yu, N.K. Shrestha, H.S. Kim, RSC Adv. 7 (2017) 6565–6573.
[27] J. Qu, Y. Yang, Q. Wu, P.R. Coxon, Y. Liu, X. He, K. Xi, N. Yuan, J. Ding, RSC Adv. 4 (2014) 11430–11437.
[28] X.D. Gao, X.M. Li, W.D. Yu, Thin Solid Films 468 (2004) 43–47.
[29] M.A. Gaikwad, M.P. Suryawanshi, S.S. Nikam, C.H. Bhosale, J.H. Kim, A.V. Moholkar, J. Photochem. Photobiol., A 329 (2016) 246–254.
[30] D. Das, P. Mondal, RSC Adv. 4.67 (2014) 35735–35743.
[31] S. Lee, H. Kim, D.J. Yun, S.W. Rhee, K. Yong, Appl. Phys. Lett. 95 (2009), 262113(1)- 262113(3).
[32] I. Pushpitasari, T.P. Gujar, K.D. Jung, O.S. Joo, Mater. Sci. Eng. B 140.3 (2007) 199–202.
[33] S.B. Jambure, S.J. Patil, A.R. Deshpande, C.D. Lokhande, Mater. Res. Bull. 49 (2014) 420–425.
[34] B. Xue, Y. Liang, L. Donglai, N. Eryong, S. Congli, F. Huanhuan, X. jingjing, J. Yong, J. Zhifeng, S. Xiaosong, Appl. Surf. Sci. 257 (2011) 10317–10321.
[35] B. Weintraub, Z. Zhou, Y. Li, Y. Deng, Nanoscale 2.9 (2010) 1573–1587.
[36] K. Zarebska, M. Kwiatkowski, M. Gniadek, M. Skompska, Electrochim. Acta 98 (2013) 255–262.
[37] J. Yang, Y.Q. Wang, J.H. Kong, H.X. Jia, Z.S. Wang, Opt. Mater. 46 (2015) 179–185.
[38] H. Chen, L. Zhu, H. Liu, W. Li, Thin Solid Films 534 (2013) 205–213.
[39] D. Polsongkram, P. Chamninok, S. Pukird, L. Chow, O. Lupan, G. Chai, H. Khallaf, S. Park, A. Schulte, Physica B 403.19 (2008) 3713–3717.
[40] C. Peng, J. Guo, W. Yang, C. Shi, M. Liu, Y. Zheng, J. Xu, P. Chen, T. Huang, Y. Yang, J. Alloy Compd. 654 (2016) 371–378.
[41] M.A. Yildirim, A. Ates, Optic Commun. 283.7 (2010) 1370–1377.
[42] A. Mortezaali, O. Taheri, Z.S. Hosseini, Microelectron. Eng. 151 (2016) 19–23.
[43] G. Calogero, A. Bartolotta, G.D. Marco, A.D. Carlo, Chem. Soc. Rev. 44.10 (2015) 3244–3294.
[44] M.M. Vadiyar, S.C. Bhise, S.K. Patil, S.S. Kolekar, A.R. Shelke, N.G. Deshpande, J.Y. Chang, K.S. Ghule, A.V. Ghule, Chem. Commun. 52 (2016) 2557–2560.
[45] C.D. Lokhande, A. Barkschat, H. Tributsch, Sol. Energy Mater. Sol. Cells 79 (2003) 293–304.

[46] D. Barpuzary, A. Banik, A.N. Panda, M. Qureshi, J. Phys. Chem. C 119.8 (2015) 3892–3902.
[47] K. Keis, E. Magnusson, H. Lindstrom, S.E. Lindquist, A. Hagfeldt, Sol. Energy Mater. Sol. Cells 73 (2002) 51–58.
[48] L. Liu, K. Hong, X. Ge, D. Liu, M. Xu, J. Phys. Chem. C 118 (2014) 15551–15555.
[49] A. Singh, D. Mohan, D.S. Ahlawat, Richa, Process. Appl. Ceram. 11 (2017) 213–219.
[50] G. Jimenez-Cadena, E. Comini, M. Ferroni, A. Vomiero, G. Sberveglieri, Mater. Chem. Phys. 124 (2010) 694–698.
[51] X. Zheng, Z. Wei, H. Chen, Y. Bai, S. Xiao, T. Zhang, S. Yang, J. Energy Chem. 24 (2015) 736–743.
[52] M. Sima, E. Vasile, M. Sima, Thin Solid Films 520 (2012) 4632–4636.
[53] G. Dai, L. Zhao, J. Li, L. Wan, F. Hu, Z. Xu, B. Dong, H. Lu, S. Wang, J. Yu, J. Colloid Interface Sci. 365.1 (2012) 46–52.
[54] C.P. Lee, P.W. Chen, C.T. Li, Y.J. Huang, S.R. Li, L.Y. Chang, P.Y. Chen, L.Y. Lin, R. Vittal, S.S. Sun, J.J. Lin, K.C. Ho, J. Power Sources 325 (2016) 209–219.
[55] E.J. Canto-Aguilar, M. Rodriguez-Perez, R. Garcia-Rodriguez, F.I. Lizama-Tzec, A.T.D. Denko, F.E. Osterloh, G. Oskam, Electrochim. Acta 258 (2017) 396–404.
[56] R. Vittal, K.C. Ho, Renew. Sustain. Energy Rev. 70 (2017) 920–935.